IEEE Access
Multidisciplinary ⋮ Rapid Review ⋮ Open Access Journal

Received December 4, 2020, accepted January 1, 2021, date of publication January 6, 2021, date of current version January 21, 2021.

Digital Object Identifier 10.1109/ACCESS.2021.3049484

Time-Domain Fault Location Algorithm for Double-Circuit Transmission Lines Connected to Large Scale Wind Farms

A. SABER[1], H. H. ZEINELDIN[1], (Senior Member, IEEE), TAREK H. M. EL-FOULY[2], (Senior Member, IEEE), AND AHMED AL-DURRA[2], (Senior Member, IEEE)

[1]Department of Electrical Power Engineering, Cairo University, Giza 12613, Egypt
[2]Advanced Power and Energy Center, Department of Electrical Engineering and Computer Science, Khalifa University, Abu Dhabi 127788, United Arab Emirates

Corresponding author: A. Saber (a_saber_86@yahoo.com)

This work was supported by the Khalifa University of Science and Technology under Award CIRA-2019-049.

ABSTRACT This article introduces a new time-domain fault location algorithm for two-terminal parallel transmission lines connected to large scale wind farms. The proposed algorithm employs only a half-cycle data window of synchronized current samples at both line terminals to avoid inaccurate estimation of current phasors due to the generated sub- and inter-harmonics currents by the wind farms. The proposed algorithm does not need any transformation method to decouple the double-circuit transmission line. Moreover, it takes into consideration the effect of the line asymmetry and the potential couplings between the six phases. The fault location equation is deduced by equalizing the differential components of the calculated instantaneous voltages at the fault point, and then the fault distance is estimated directly without any iterative algorithm. The two-terminal parallel transmission line is emulated by PSCAD/EMTDC platform utilizing the frequency-dependent phase model, and the required calculations for fault location are conducted by MATLAB software. The proposed algorithm is tested for several fault resistances and fault locations, and all fault types, including cross-circuit faults. In addition, the effect of measurement, synchronization, and line parameters errors on the fault location accuracy is investigated. The obtained results confirm acceptable accuracy of the proposed fault location algorithm.

INDEX TERMS Domain fault location, double-circuit transmission line, large scale wind farms, current samples.

I. INTRODUCTION

Double-circuit transmission lines are widely employed for power transmission systems. Fault location estimation for double-circuit lines is more complex than that for single-circuit lines due to the existing potential couplings between the parallel circuits and the occurrence possibility of cross-circuit faults. Various fault location algorithms have been proposed for transmission lines [1], [2]. Their principles and adopted algorithms have been introduced in [3], which include traveling-wave based schemes, high-frequency components based schemes, knowledge-based schemes, and frequency-domain based schemes. Both traveling-wave and high-frequency components based schemes are more complex and expensive as they are based on a high sampling frequency and especially tuned filters for high-frequency components measurements, respectively [3]. In addition, knowledge-based schemes initially require manual training process, and they are not applicable to new transmission lines without performing a new training process [3]. Moreover, frequency-domain based fault location schemes are a well-known method in literature for double-circuit transmission lines [4]–[10]. One of the main challenges for such schemes is the accurate estimation of voltage and current phasors at line terminals, especially during the fault transient. Therefore, a long data window after fault instant may be necessary to estimate the phasors accurately, and consequently, the fault location. However, a long data window may not be available in case of using high-speed tripping protective relay [11], [12]. In addition, for transmission lines connected

The associate editor coordinating the review of this manuscript and approving it for publication was Flavia Grassi.

to large scale wind farms, the fault characteristics of the wind turbine generators are completely different from those of the synchronous generators [13]. Furthermore, the phasors may be estimated inaccurately due to the negative effect of the generated sub- and inter-harmonics by the wind farms, especially during the fault transient [14].

Considering the above reasons, time-domain based fault location schemes, which utilize a short data window, have been introduced for transmission lines [12], [15]–[17]. In [12], a time-domain fault location scheme has been proposed using current samples. In this scheme, the double-circuit line is decoupled into the differential component and the common component where the differential component is utilized for fault location calculations. In [15], a time–time-transform-based fault location scheme has been introduced for three-terminal single- and double-circuit transmission lines. In this scheme, a time-time transformation is used to determine the arrival time of the travelling waves, which is used to estimate the fault location. Both schemes [12], [15] have high fault location accuracy for a higher sampling rate. However, the fault location accuracy for both schemes decrease with the decrease in sampling rate. In addition, the line asymmetry has a negative influence on the fault location accuracy of both schemes, especially for double-circuit lines due to the mutual coupling effect between both circuits. Furthermore, the scheme in [12] is not applicable for cross-circuit faults. In [16], a time-domain fault location scheme has been proposed for single-circuit transmission lines. In this scheme, a minimum sampling rate of 40 kHz is required. In addition, its fault location accuracy is negatively affected by the sampling rate and the errors in line parameters. In [17], a time-domain fault location scheme has been proposed for double-circuit transmission lines utilizing on-terminal current measurements. However, it may become difficult to estimate accurately the fault distance in the absence of the measurements from the other line terminal due to the negative effect of several factors, such as loading conditions, fault infeed from other end, and variable source impedances. In addition, the errors in line parameters have a significant impact on the fault location accuracy of the one-end fault location schemes.

For transmission lines connected to large scale wind farms, Several fault detection schemes have been proposed to overcome the over-reach and under-reach problems associated with the distance protection for these lines connected to large scale wind farms, such as [18]–[22]. However, only two time-domain based fault location schemes have been introduced for single-circuit transmission lines [23], [24]. In [23], wireless communication links are utilized to transfer the measured voltage and current signals from one end of the line to the other end. In addition, a half-cycle post-fault data window is used for fault location calculations. This scheme requires a sampling frequency of 20 kHz. In [24], fast discrete S-transform is used to detect the arrival time of the first travelling wave of the currents at each terminal. However, this scheme requires a high sampling frequency of 200 kHz, which may not be applicable practically.

For double-circuit transmission lines connected to a large scale wind farms, only an adaptive distance relay setting has been proposed in [25]. However, the fault location issue is not introduced in this article. In Egypt, there are two large scale wind farms at Gulf of Suez (Ras Ghareb) station and Gabal El-Zeit station, which are connected to the Egyptian grid through double-circuit transmission lines with line lengths of 50 km and 280 km, respectively [26]. Recently, the average rated capacity of the installed offshore wind turbines reached up to 8.4 MW [27], and the first prototype of the largest onshore wind turbine (12 MW) has been installed at the Port of Rotterdam in 2019 [27]. Consequently, with the increasing power capacity of the large scale wind farms, the double-circuit transmission line is an available option for interconnection with main grid.

In this article, a time-domain fault location algorithm is proposed for two-terminal parallel transmission lines connected to large scale wind farms. The double-circuit line is simulated using the PSCAD/EMTDC software utilizing the frequency-dependent phase model. The main advantages of the proposed algorithm are:

- A half-cycle of the post-fault current samples at both line terminals is only required for fault location calculations, and there is no need for any transformation technique to decouple the double-circuit transmission line.
- The fault location equation is derived considering the line asymmetry and the mutual coupling between all phases.
- The fault distance is calculated directly using a non-iterative equation, and the computational burden is negligible.

The proposed algorithm is tested considering several fault resistances up to 100 Ω and fault locations. The locations of all types of faults, including cross-circuit faults, are considered. Furthermore, the effect of different sampling rates, synchronization and line parameters errors on the performance of the proposed fault localization algorithm is investigated.

This article is organized as follows. The modeled power system and the derived fault location equation are discussed in Section II. In addition, the implementation of the proposed fault location algorithm is shown in Section III. Furthermore, the simulated results are presented in Section IV, and this article is summarized in Section V.

II. PROPOSED FAULT LOCATION ALGORITHM

In the next subsections, the simulated power system is introduced in Sub-section II.A, and the deduction of the fault location equation is presented in Sub-section II.B.

A. SIMULATED POWER SYSTEM

Fig. 1 shows the 220 kV, 60 Hz, $D_{SR} = 150$ km parallel transmission line connected between terminals S and R.

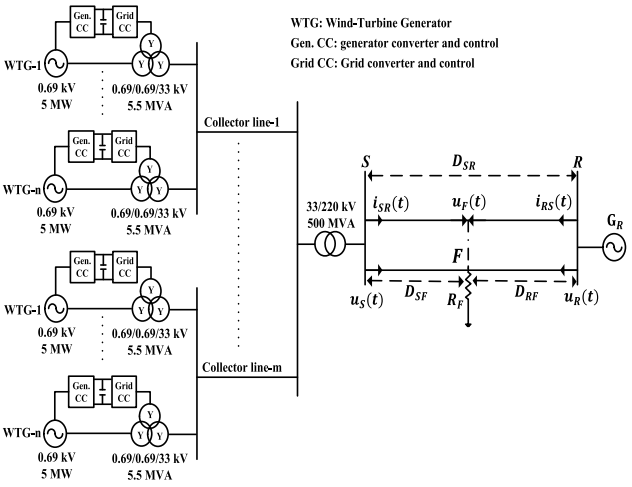

FIGURE 1. Modeled Power System.

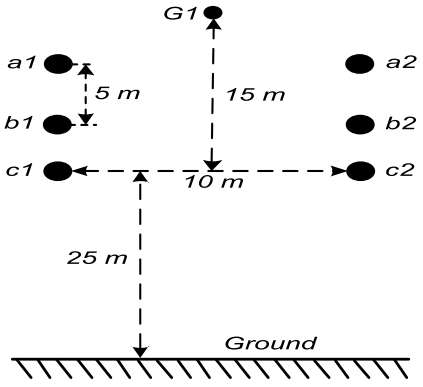

FIGURE 2. Tower specifications for parallel transmission line.

The wind farm is connected to terminal S through step-up transformer, and it consists of a type-3 double-fed wound rotor induction generator and an AC-DC-AC voltage source converter. More detailed information regarding the controllers of both grid and rotor sides, the crowbar circuit protection, and the DC-link chopper are given in [28]. The power capacity of the wind farm is equal to 300 MW (60 × 5 MW), and the step-up transformer is 33/220 kV, 500 MVA, and Yg/Yg solidly grounded connection with leakage reactance of 10%. The main information of the wind-turbine generator is presented in Appendix A, and the rating of the wind-turbine transformer is 0.69/0.69/33 kV, 5.5 MVA, and Yg/Yg/Yg solidly grounded connection. In addition, the current transformers (CTs) are simulated considering its characteristics and the data of the CTs are presented in Appendix B. Further, the system source parameters at terminal R and the line parameters matrices considering the untransposition of the double-circuit line are given in Appendix C and Appendix D, respectively. The tower configuration of the parallel line (S-R) is depicted in Fig. 2.

B. DEDUCTION OF THE FAULT LOCATION EQUATION

In [11], a fault location algorithm has been introduced for single-circuit transmission lines. However, the synchronized voltage and current samples at both line ends are required to deduce the fault location equation. In addition, all line parameters (line resistance, inductance, and capacitance) are required, and the effect of the errors in line parameters is not investigated. Furthermore, in case of long lines, iteration method is required to estimate the fault distance. On the other hand, the proposed fault location algorithm utilizes only the synchronized current samples at both line ends, and the line shunt capacitance is not required. In addition, the fault distance is obtained directly using non-iterative equation, and the computational burden is negligible, as explained later in this subsection. Moreover, the performance of the proposed algorithm is robust against the errors in line parameters, as shown later in Subsection IV.D.

Consider a generic fault at a distance of D_{SF} away from terminal S and D_{RF} away from terminal R, as shown in Fig. 1. Considering the line shunt capacitance, the instantaneous voltage in time-domain at fault point ($u_{FS}(t)$) is written as:

$$u_{FS}(t) = u_{SR}(t) - D_{SF} \times \left\{ R \times i_{SF}(t) + L \times \frac{d\left[i_{SF}(t)\right]}{dt} \right\} \tag{1}$$

where $i_{SF}(t)$ is equal to:

$$i_{SF}(t) = i_{SR}(t) - \frac{1}{2} \times D_{SF} \times C \times \frac{d\left[u_{SR}(t)\right]}{dt} \tag{2}$$

where the dimensions of both instantaneous phase voltages $\{u_{FS}(t)$ and $u_{SR}(t)\}$ and currents $\{i_{SF}(t)$ and $i_{SR}(t)\}$ are 6×1. R, L, and C are respectively, resistance, inductance, and capacitance matrices of the line (S-R) per-unit length, and they are equal to:

$$R = \begin{bmatrix} R_{a1,a1} & R_{a1,b1} & R_{a1,c1} & R_{a1,a2} & R_{a1,b2} & R_{a1,c2} \\ R_{b1,a1} & R_{b1,b1} & R_{b1,c1} & R_{b1,a2} & R_{b1,b2} & R_{b1,c2} \\ R_{c1,a1} & R_{c1,b1} & R_{c1,c1} & R_{c1,a2} & R_{c1,b2} & R_{c1,c2} \\ R_{a2,a1} & R_{a2,b1} & R_{a2,c1} & R_{a2,a2} & R_{a2,b2} & R_{a2,c2} \\ R_{b2,a1} & R_{b2,b1} & R_{b2,c1} & R_{b2,a2} & R_{b2,b2} & R_{b2,c2} \\ R_{c2,a1} & R_{c2,b1} & R_{c2,c1} & R_{c2,a2} & R_{c2,b2} & R_{c2,c2} \end{bmatrix} \tag{3}$$

$$L = \begin{bmatrix} L_{a1,a1} & L_{a1,b1} & L_{a1,c1} & L_{a1,a2} & L_{a1,b2} & L_{a1,c2} \\ L_{b1,a1} & L_{b1,b1} & L_{b1,c1} & L_{b1,a2} & L_{b1,b2} & L_{b1,c2} \\ L_{c1,a1} & L_{c1,b1} & L_{c1,c1} & L_{c1,a2} & L_{c1,b2} & L_{c1,c2} \\ L_{a2,a1} & L_{a2,b1} & L_{a2,c1} & L_{a2,a2} & L_{a2,b2} & L_{a2,c2} \\ L_{b2,a1} & L_{b2,b1} & L_{b2,c1} & L_{b2,a2} & L_{b2,b2} & L_{b2,c2} \\ L_{c2,a1} & L_{c2,b1} & L_{c2,c1} & L_{c2,a2} & L_{c2,b2} & L_{c2,c2} \end{bmatrix} \tag{4}$$

$$C = \begin{bmatrix} C_{a1,a1} & C_{a1,b1} & C_{a1,c1} & C_{a1,a2} & C_{a1,b2} & C_{a1,c2} \\ C_{b1,a1} & C_{b1,b1} & C_{b1,c1} & C_{b1,a2} & C_{b1,b2} & C_{b1,c2} \\ C_{c1,a1} & C_{c1,b1} & C_{c1,c1} & C_{c1,a2} & C_{c1,b2} & C_{c1,c2} \\ C_{a2,a1} & C_{a2,b1} & C_{a2,c1} & C_{a2,a2} & C_{a2,b2} & C_{a2,c2} \\ C_{b2,a1} & C_{b2,b1} & C_{b2,c1} & C_{b2,a2} & C_{b2,b2} & C_{b2,c2} \\ C_{c2,a1} & C_{c2,b1} & C_{c2,c1} & C_{c2,a2} & C_{c2,b2} & c_{c2,c2} \end{bmatrix} \tag{5}$$

where a_1, b_1, c_1, a_2, b_2, and c_2 denote the phases of circuit-1 and circuit-2, respectively. As the instantaneous voltage at the end $S(u_{SR}(t))$ of similar phases in both circuits are equal. Therefore, the differential component of similar phases in both circuits for the instantaneous voltage ($u_{SR}(t)$) and its

derivative $\left\{\frac{d[u_{SR}(t)]}{dt}\right\}$ are equal to zero:

$$\begin{bmatrix} u_{SR,a1}(t) - u_{SR,a2}(t) \\ u_{SR,b1}(t) - u_{SR,b2}(t) \\ u_{SR,c1}(t) - u_{SR,c2}(t) \end{bmatrix} = \begin{bmatrix} 0 \\ 0 \\ 0 \end{bmatrix} \;\&\; \Delta\left\{\frac{d\,[u_{SR}(t)]}{dt}\right\} = 0 \tag{6}$$

Equation (1) is rewritten after subtracting similar phases in both circuits of the instantaneous voltage ($u_{FS}(t)$) from each other:

$$\Delta u_{FS}(t) = -D_{SF} \times \left\{\Delta R \times \Delta i_{SF}(t) + \Delta L \times \Delta\left\{\frac{d[i_{SF}(t)]}{dt}\right\}\right\} \tag{7}$$

where $\Delta u_{FS}(t)$, $\Delta i_{SF}(t)$, ΔR, and ΔL are equal to:

$$\Delta u_{FS}(t) = \begin{bmatrix} u_{FS,a1}(t) - u_{FS,a2}(t) \\ u_{FS,b1}(t) - u_{FS,b2}(t) \\ u_{FS,c1}(t) - u_{FS,c2}(t) \end{bmatrix} \;\&$$

$$\Delta u_{FS}(t) = \begin{bmatrix} i_{SF,a1}(t) - i_{SF,a2}(t) \\ i_{SF,b1}(t) - i_{SF,b2}(t) \\ i_{SF,c1}(t) - i_{SF,c2}(t) \end{bmatrix} \tag{8}$$

$$\Delta R = \begin{bmatrix} R_{a1,a1} - R_{a1,a2} & R_{a1,b1} - R_{a1,b2} & R_{a1,c1} - R_{a1,c2} \\ R_{b1,a1} - R_{b1,a2} & R_{b1,b1} - R_{b1,b2} & R_{b1,c1} - R_{b1,c2} \\ R_{c1,a1} - R_{c1,a2} & R_{c1,b1} - R_{c1,b2} & R_{c1,c1} - R_{c1,c2} \end{bmatrix} \tag{9}$$

$$\Delta L = \begin{bmatrix} L_{a1,a1} - L_{a1,a2} & L_{a1,b1} - L_{a1,b2} & L_{a1,c1} - L_{a1,c2} \\ L_{b1,a1} - L_{b1,a2} & L_{b1,b1} - L_{b1,b2} & L_{b1,c1} - L_{b1,c2} \\ L_{c1,a1} - L_{c1,a2} & L_{c1,b1} - L_{c1,b2} & L_{c1,c1} - L_{c1,c2} \end{bmatrix} \tag{10}$$

Equation (2) is also rewritten:

$$\Delta i_{SF}(t) = \Delta i_{SR}(t) = \begin{bmatrix} i_{SR,a1}(t) - i_{SR,a2}(t) \\ i_{SR,b1}(t) - i_{SR,b2}(t) \\ i_{SR,c1}(t) - i_{SR,c2}(t) \end{bmatrix} \tag{11}$$

Accordingly, equation (7) is rewritten as follows:

$$\Delta u_{FS}(t) = -D_{SF} \times \left\{\Delta R \times \Delta i_{SR}(t) + \Delta L \times \Delta\left\{\frac{d\,[i_{SR}(t)]}{dt}\right\}\right\} \tag{12}$$

Similarly, the differential component of the similar phases in both circuits for the instantaneous voltage ($\Delta u_{FR}(t)$) is equal to:

$$\Delta u_{FR}(t) = -D_{RF} \times \left\{\Delta R \times \Delta i_{RS}(t) + \Delta L \times \Delta\left\{\frac{d\,[i_{RS}(t)]}{dt}\right\}\right\} \tag{13}$$

From Kirchhoff voltage law, both variables ($\Delta u_{FS}(t)$ and $\Delta u_{FR}(t)$) must be equal to each other at the fault point. Accordingly:

$$(D_{SR} - D_{RF}) \times \left\{\Delta R \times \Delta i_{SR}(t) + \Delta L \times \Delta\left\{\frac{d\,[i_{SR}(t)]}{dt}\right\}\right\} = D_{RF} \times \left\{\Delta R \times \Delta i_{RS}(t) + \Delta L \times \Delta\left\{\frac{d\,[i_{RS}(t)]}{dt}\right\}\right\} \tag{14}$$

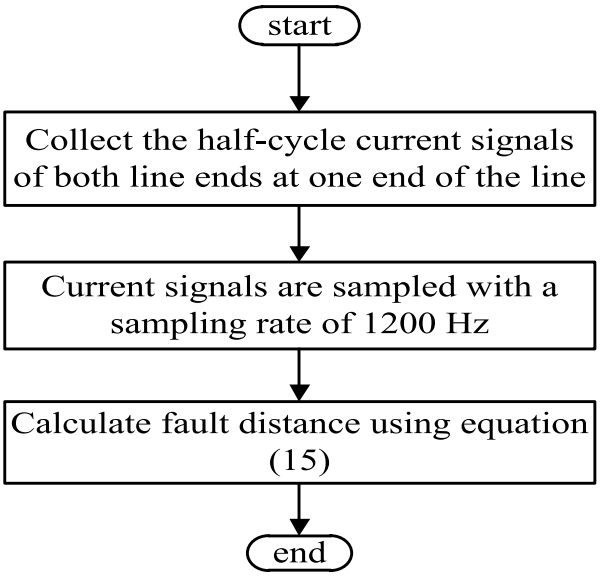

FIGURE 3. Steps of the proposed fault location algorithm.

It can be noted that if the instantaneous currents samples at both terminals of the transmission line are measured during the fault transient, the fault distance (L_{RF}) can be calculated from (15), as shown at the bottom of the next page.

III. IMPLEMENTATION OF THE FAULT LOCATION ALGORITHM

Practically, fault location calculations are performed offline since the results of these calculations are required for human users. Therefore, the communication delay is more critical for fault detection, and it is required to reduce the communication time delay as much as possible to isolate the faulted zone as fast as possible. On the other hand, in the case of fault location, the speed of the calculations can be measured in seconds or even minutes [3]. The procedure for the proposed fault location algorithm can be summarized in the following three points:

1) The measured current signals at both line ends are collected at one end of the line.

2) The current signals are sampled with a sampling rate of 1200 Hz. The influence of the sampling frequency (F_S) on the fault location accuracy is discussed in the next section.

3) Equation (14) can be written in discrete form, as shown in (15), where n is the number of samples, and T is the sampling time. It can be noted that two samples of the instantaneous currents can be used to obtain the fault location. However, to get more accurate results, a half-cycle (10 samples for $F_S = 1200$ Hz) is considered in fault location calculations. The steps of the fault location algorithm are shown in Fig. 3.

In case of false tripping, the double-circuit line is healthy. Therefore, the differential current components of similar phases in both circuits will be equal to zero at each line end because the phase currents of similar phases in both circuits will be equal to each other. Accordingly, both sides of equation (15) will be equal to zero, and equation (15) will

not be applicable in this case. In addition, It is worth noting that the proposed algorithm is applicable only as long as both circuits of the double-circuit line are in service, and it can not be applied if one of the two circuits is out-of-service.

IV. PERFORMANCE EVALUATION

The power system depicted in Fig. 1 is emulated using PSCAD/EMTDC software, and the required fault location analysis is executed using MATLAB software. Several fault cases are carried out by changing the fault resistance (R_F), fault location, and fault inception angle (δ_F). All single- and cross-circuit fault types are simulated. The current signals at both line ends are sampled with a sampling rate of 1200 Hz, and the nominal wind speed is equal to 11 m/sec. All test cases in the following subsections are simulated at the nominal wind speed, unless it is stated otherwise. The fault location error is computed from [2]–[7]:

$$Error\% = \frac{|calculated\ length - actual\ length|}{L_{SR}} \times 100\% \tag{16}$$

A. DIFFERENT FAULT TYPES

Number Twelve test cases are shown in Table 1 for all fault types, including single- and cross-circuit faults. Different fault locations, fault resistances, fault inception angles are taken into account. In the last two columns in Table 1, the estimated fault distance away from terminal R (D_F) and the absolute fault location percentage error (F.L. error %) are presented. The first four-cases are single-circuit faults in circuit-1, the next four cases are single-circuit faults in circuit-2, and the last four cases are cross-circuit faults. For example, the eighth case in Table 1 represents a three-phase fault in circuit-2 ($a_2b_2c_2$) with $\delta_F = 135°$, $L_{RF} = 0.2$ per-unit, and $R_F = 40\Omega$. The current waveforms of circuit-2 at both line ends are shown in Fig. 4. It is assumed that the fault is detected, and the circuit breaker is completely opened within two cycles, which is considered the case of using high-speed tripping protective relays [11], [12]. The last half-cycle before opening the circuit breaker is utilized in (15) to estimate the fault location. Solving (15), the obtained fault distance is 0.2007 per-unit, and the absolute fault location percentage error is 0.07% (0.105 km). Another example, the last case

TABLE 1. Results for different fault cases.

Test Case				D_F (p.u.)	F.L. error (km)	F.L. error%
Fault Type	δ_F°	L_{RF} (p.u.)	R_F (Ω)			
c_1g	180	0.3	20	0.3003	0.045	0.03
a_1c_1	90	0.7	1	0.7000	0.000	0.00
b_1c_1g	135	0.9	100	0.8992	0.120	0.08
$a_1b_1c_1$	45	0.05	0.1	0.0521	**0.315**	**0.21**
b_2g	0	0.15	5	0.1504	0.060	0.04
b_2c_2	90	0.4	0.01	0.4000	0.000	0.00
a_2c_2g	180	0.6	90	0.5998	0.030	0.02
$a_2b_2c_2$	135	0.2	40	0.2007	0.105	0.07
b_1g-c_2g	0	0.25	10	0.2505	0.075	0.05
a_1g-b_2g	45	0.8	50	0.7998	0.030	0.02
a_1b_1g- a_2c_2g	180	0.1	0.01	0.1005	0.075	0.05
b_1c_1g- a_2b_2g	90	0.5	80	0.5000	0.000	0.00

represents a cross-circuit fault (b_1c_1g- a_2b_2g) in both circuits with $\delta_F = 90°$, $L_{RF} = 0.5$ per-unit, and $R_F = 80\Omega$. Solving (15), the obtained fault distance is 0.50 per-unit, and the absolute F.L. error% is 0.0%. Further, the maximum recorded error is 0.21% (0.315 km), and the average percentage error of the twelve cases is 0.048%. As shown in table 1, the obtained accuracy of the fault location is quite acceptable for single- and cross-circuit faults.

B. EFFECT OF FAULT RESISTANCE AND SAMPLING RATE

Different cases are simulated to investigate the effect of different fault resistances at different sampling rates. The results are depicted in Fig. 5 for a single-phase a_1 to ground fault in circuit-1 (a_1g). Different fault locations are considered with step 10% of the line length, and four values for fault resistance (0.1, 1, 10, and 100 Ω) are considered. The fault inception angle is set at 90°. As shown, the fault location error decreases to approximately zero when the fault occurs at the middle of the line. This is due to the nature of the fault location equation in (15). At the middle of the line, the parts inside the round bracket { } in both sides of (15) are approximately equal to each other, and the calculated fault distance is equal to 0.5 per-unit in this case. In addition, the absolute F.L. error%

$$\begin{aligned}
&(D_{SR} - D_{RF}) \\
&\quad \times \left\{ \Delta R \times \begin{bmatrix} i_{SR,a1}(nT) - i_{SR,a2}(nT) \\ i_{SR,b1}(nT) - i_{SR,b2}(nT) \\ i_{SR,c1}(nT) - i_{SR,c2}(nT) \end{bmatrix} + \frac{\Delta L}{T} \times \begin{bmatrix} i_{SR,a1}(nT) - i_{SR,a2}(nT) - i_{SR,a1}[(n-1)T] + i_{SR,a2}[(n-1)T] \\ i_{SR,b1}(nT) - i_{SR,b2}(nT) - i_{SR,b1}[(n-1)T] + i_{SR,b2}[(n-1)T] \\ i_{SR,c1}(nT) - i_{SR,c2}(nT) - i_{SR,c1}[(n-1)T] + i_{SR,c2}[(n-1)T] \end{bmatrix} \right\} \\
&= D_{RF} \times \left\{ \Delta R \times \begin{bmatrix} i_{RS,a1}(nT) - i_{RS,a2}(nT) \\ i_{RS,b1}(nT) - i_{RS,b2}(nT) \\ i_{RS,c1}(nT) - i_{RS,c2}(nT) \end{bmatrix} + \frac{\Delta L}{T} \right. \\
&\qquad \left. \times \begin{bmatrix} i_{RS,a1}(nT) - i_{RS,a2}(nT) - i_{RS,a1}[(n-1)T] + i_{RS,a2}[(n-1)T] \\ i_{RS,b1}(nT) - i_{RS,b2}(nT) - i_{RS,b1}[(n-1)T] + i_{RS,b2}[(n-1)T] \\ i_{RS,c1}(nT) - i_{RS,c2}(nT) - i_{RS,c1}[(n-1)T] + i_{RS,c2}[(n-1)T] \end{bmatrix} \right\}
\end{aligned} \tag{15}$$

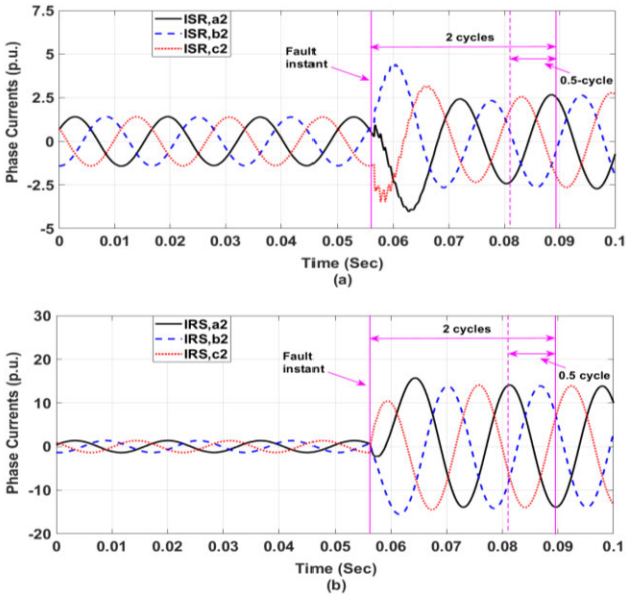

FIGURE 4. Current waveforms of circuit-2 at both line ends due to $a_2b_2c_2$ fault.

is less than 0.1% in most fault cases. The maximum absolute percentage errors are 0.07%, 0.067%, 0.084%, and 0.105% for fault resistance of 0.1, 1, 10, and 100 Ω, respectively. Further, the maximum absolute percentage errors are 0.078%, 0.085%, 0.088%, and 0.105% for sampling rates of 1.2, 2.4, 4.8, and 9.6 kHz, respectively. It can be noted that the fault location accuracy is acceptable for wide range of fault resistance, and changing the sampling rate has a slight effect on the fault location accuracy.

C. EFFECT OF WIND SPEED VARIATIONS

Different cases are simulated to investigate the effect of wind speed variations. The results are depicted in Fig. 6 for a double-phase to ground fault in circuit-2 (a_2b_2g) with different fault locations (step 10% of the line length) and four values of the fault resistance (0.1, 1, 10, and 100 Ω). The fault inception angle is set at 180°. As shown, the maximum absolute percentage errors are 0.129%, 0.136%, 0.133%, and 0.145% for wind speed of 4, 8, 12, and 16 m/sec, respectively. The average absolute percentage errors are 0.05%, 0.0508%, 0.053%, and 0.054% for wind speed of 4, 8, 12, and 16 m/sec, respectively. It can be concluded that the proposed algorithm shows a satisfactory performance by considering the variations of the wind speed.

D. EFFECT OF LINE PARAMETERS ERRORS

One of the main advantages of the proposed algorithm is that the introduced errors in line parameters have a slight effect on the fault location accuracy due to the nature of the fault location equation in (15). Mathematically, any increase or decrease in line resistance (R) and line inductance (L) matrices will be reflected in the difference of ΔR and ΔL in both sides of equation (15). Therefore, the line parameters errors have a negligible influence on the obtained results of the proposed algorithm. To model the line parameter errors, ±50% errors are considered in the line parameters utilized for fault location estimation. The absolute fault location errors are shown in Fig. 7 for a double-phase fault (a_1c_1) in circuit-1 with different fault locations and fault resistances. The fault inception angle is set at 0°. The maximum and average absolute percentage errors for all cases are 0.1776% and 0.0443%, respectively. It is worth noting the same results are obtained without including the line parameter errors.

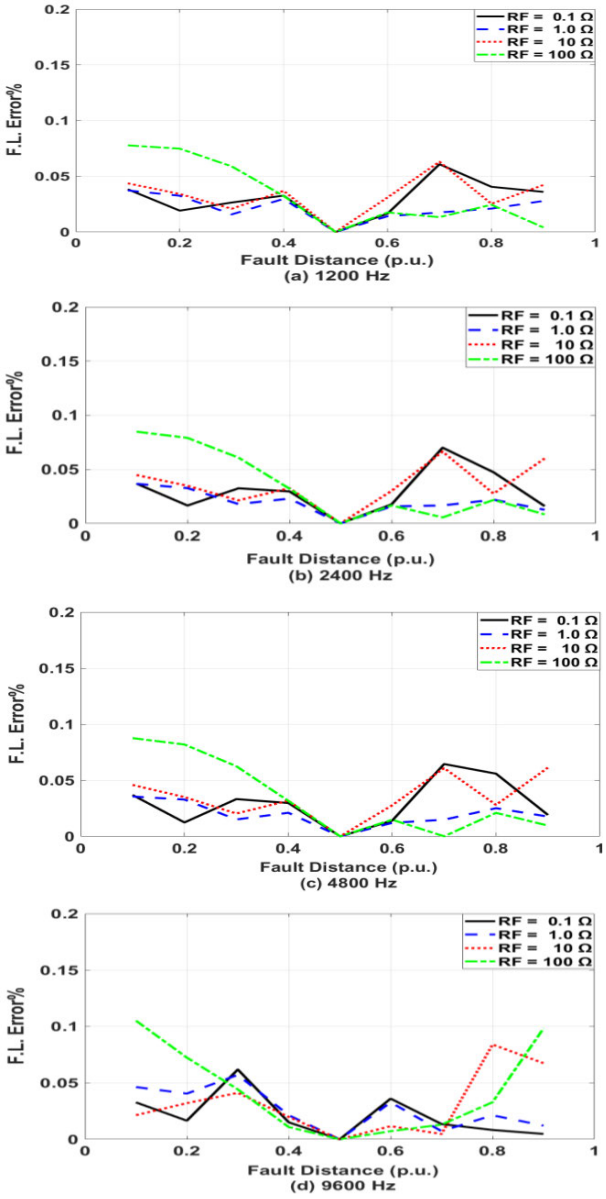

FIGURE 5. F.L. error for different fault resistances at different sampling rates.

E. EFFECT OF MEASUREMENT AND TIME SYNCHRONIZATION ERRORS

To study the effect of the measurement errors (MEs), ±5 MEs are considered in the current samples. ME of +5% is considered at one line terminal, while ME of −5% is considered at

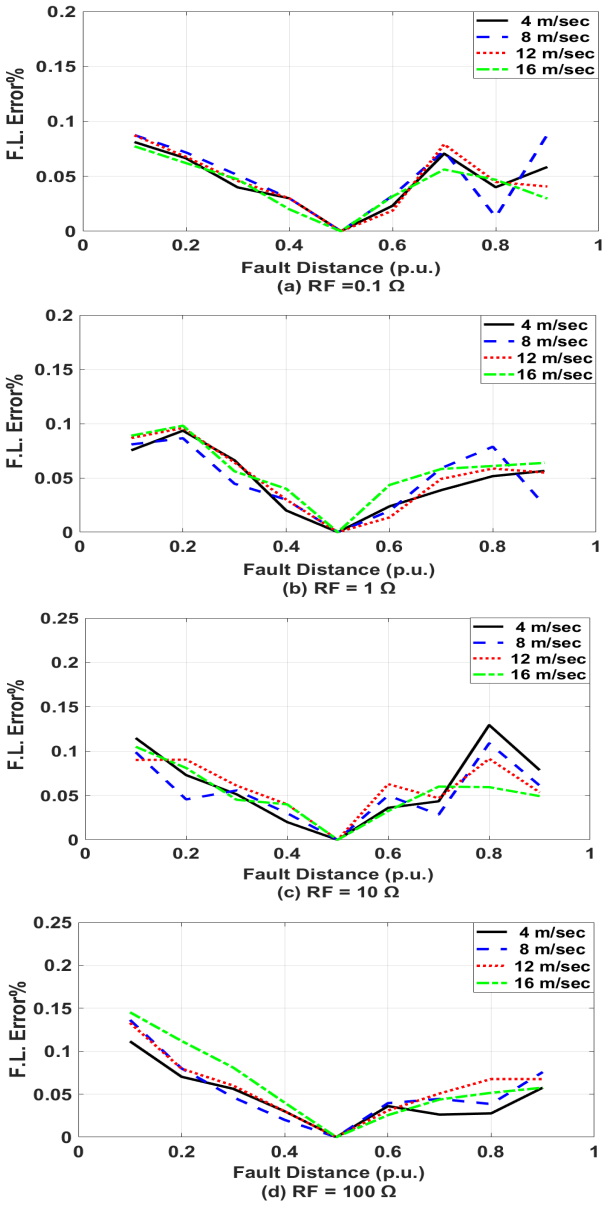

FIGURE 6. F.L. error for different wind speed at different fault resistances.

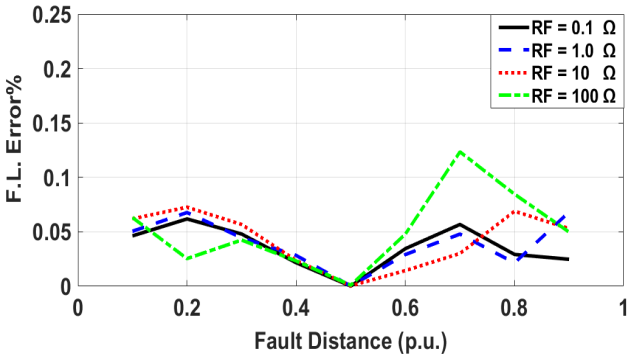

FIGURE 7. F.L. error for ±50% errors in line parameters at different fault resistances.

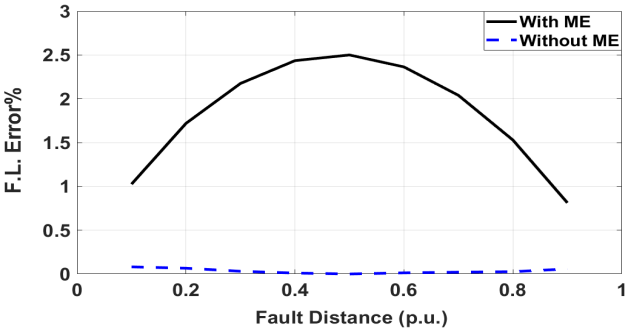

FIGURE 8. F.L. error with/without considering measurement error (ME) of ±5% at different fault distances.

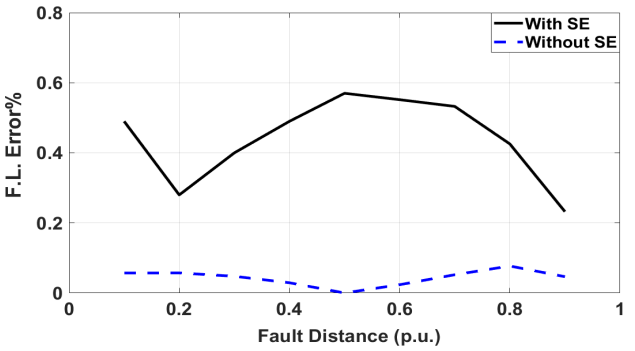

FIGURE 9. F.L. error with/without considering synchronization error (SE) of 9° at different fault distances.

the other line terminal. The results are shown in Fig. 8 for a single-phase to ground fault in circuit-1 (b_1g) at different fault distances, $R_F = 1\Omega$, and $\delta_F = 135°$. As shown, the maximum and average absolute percentage errors are respectively equal to 0.081% and 0.034% without considering the effect of the MEs. On the other hand, the maximum and average absolute percentage errors are respectively equal to 2.50% and 1.844% considering the effect of the MEs.

In addition, a synchronization time error of 0.41667 msec $\left(= \frac{1}{2400} m\,\text{sec}\ \ or\ 9°\right)$ is considered between the current samples of both sides of the line. The results are shown in Fig. 9 for a three-phase fault in circuit-2 ($a_2b_2c_2$) at different fault distances, $R_F = 10\Omega$, and $\delta_F = 45°$. As shown, the maximum and average absolute percentage errors are respectively equal to 0.077% and 0.046% without considering the effect of the synchronization errors (SEs). On the other hand, the maximum and average absolute percentage errors are respectively equal to 0.57% and 0.44% considering the effect of the SEs. It can be concluded that the accuracy of the fault location is still within an acceptable range taking into consideration the effect of MEs and SEs.

F. EFFECT OF DIFFERENT LINE LENGTHS AND TYPE-4 WIND FARM

The line length is equal to 150 km in previous results. The behavior of the proposed fault location algorithm is investigated for different line lengths of 50 km and 300 km, respectively. The cases in Table 1 are repeated at the same conditions and results are depicted in Table 2 for both line lengths (50 km

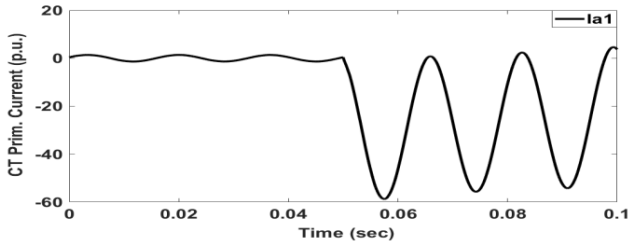

FIGURE 10. CT primary current for a bolted three-phase at 5% of the line length.

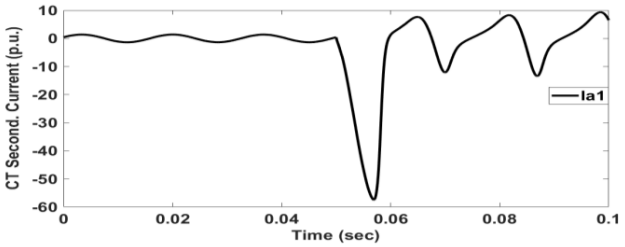

FIGURE 11. CT secondary current for a bolted three-phase fault at 5% of the line length.

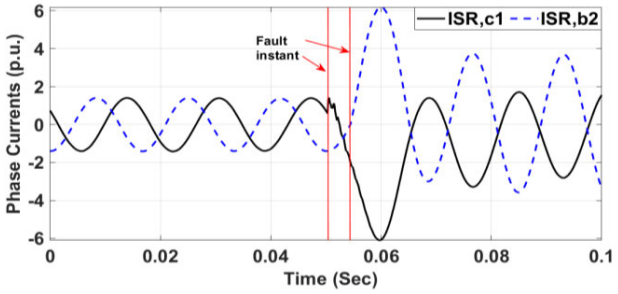

FIGURE 12. Current waveforms of the faulty phases at the line end S line ends due to evolving fault.

and 300 km). As shown, the maximum absolute percentage errors are equal to 0.03% and 0.48% for 50 km and 300 km, respectively. The average percentage errors of these cases are equal to 0.007% and 0.163% for 50 km and 300 km, respectively.

In previous results, type-3 wind turbine model is utilized. The response of the proposed fault location algorithm is also demonstrated for type-4 wind turbine model. The power capacity of the wind farm is equal to 450 MW (90 × 5 MW). The detailed type-4 wind turbine model, including the mechanical and the electrical components is given in [29]. Table 2 presents the absolute percentage error for the same cases in Table 1 at the same conditions. The maximum and average absolute percentage errors are equal to 0.24% and 0.056%, respectively. The obtained results prove the applicability of the proposed fault location algorithm for different line lengths and different types of wind turbines.

G. EFFECT OF CURRENT TRANSFORMER (CT) SATURATION

CT calculations are normally carried out to assure that the CT will not saturate in the case of external faults [30]. On the other hand, it is expected that the CT may saturate in the case of severe internal faults. The main factor, which affects the saturation characteristic of the CT, is the secondary side burden resistance of the CT, where the probability of CT saturation is proportional to the value of this burden resistance. The value of the burden resistance is set at 2 Ω in previous results. To show the impact of CT saturation, the value of the burden resistance is set at 4 Ω, and a bolted three-phase fault in circuit-1 ($a_1b_1c_1$) at 5% of the line length is conducted with $\delta_F = 0°$. The primary and secondary current waveforms of the CT corresponding to phase a_1 at the line end near to the fault point are shown in Fig. 10 and Fig. 11, respectively, where the CT saturates within 10 msec after fault instant. Solving (15), the obtained fault distance is equal to 0.0512 per-unit, and the absolute fault location percentage error is 0.12% (180 meters). As shown, the CT Saturation has a slight effect on the accuracy of the proposed algorithm.

H. EFFECT OF NOISE AND EVOLVING FAULTS

To consider the noise effect, the signal-to-noise ratio is normally in the range of 40-60 dB in recent literature [31]. Accordingly, the cases in Table 1 are repeated at the same fault conditions, and Gaussian noise with a signal-to-noise ratio of 40 dB is added to the current signals. The new results considering the noise effect are depicted in Table 3. As shown, the maximum absolute percentage errors are equal to 0.22% and 0.21% with and without considering the noise effect, respectively. The average percentage errors of these cases are equal to 0.09% and 0.05% with and without considering the noise effect, respectively.

To demonstrate the effect of the evolving faults, a single-phase to ground fault in circuit-1 (c_1g) is simulated at 30% of line length with $R_F = 1\Omega$ and $\delta_F = 0°$. Another single-phase to ground fault in circuit-2 (b_2g) is simulated at the same location with $R_F = 10\Omega$ and $\delta_F = 90°$. The current waveforms of the faulty phases at the line end S are shown in Fig. 12. Solving (15), the obtained fault distance is equal to 0.3005 per-unit, and the absolute fault location percentage error is 0.05% (75 meters). It can be concluded that the proposed algorithm achieves high accuracy considering the effect of the noise and evolving faults.

I. COMPARATIVE EVALUATION WITH PREVIOUS SCHEMES APPLIED TO TRANSMISSION LINES CONNECTED TO LARGE SCALE Wind FARMS

The proposed fault location algorithm is evaluated with respect to recent time-domain fault location schemes in literature [23], [24], which are applied to transmission lines connected to large scale wind farms, as shown in Table 4. This can be illustrated in the following points:

- The proposed algorithm is applied to double-circuit line and the frequency-dependent line model is used to simulate the double-circuit line. The schemes in [23], [24] are applied to single-circuit line, and the line is simulated using the lumped parameter line model.

TABLE 2. Results for type-4 WTG and line lengths of 50 km and 150 km.

L_{RF} (p.u.)	50 km		300 km		Type-4 WTG	
	D_F (p.u.)	F.L. error%	D_F (p.u.)	F.L. error%	D_F (p.u.)	F.L. error%
0.3	0.3001	0.01	0.3024	0.24	0.3001	0.01
0.7	0.7000	0.00	0.6952	**0.48**	0.7006	0.06
0.9	0.8993	**0.03**	0.9002	0.02	0.9008	0.08
0.05	0.0499	0.01	0.0511	0.11	0.0501	0.01
0.15	0.1500	0.00	0.1505	0.05	0.1500	0.00
0.4	0.4000	0.00	0.4015	0.15	0.4009	0.09
0.6	0.6001	0.01	0.6004	0.04	0.5976	**0.24**
0.2	0.2000	0.00	0.2022	0.22	0.2006	0.06
0.25	0.2500	0.00	0.2522	0.22	0.2505	0.05
0.8	0.8001	0.01	0.7980	0.2	0.7998	0.02
0.1	0.1001	0.01	0.1023	0.23	0.1005	0.05
0.5	0.5000	0.00	0.5000	0.00	0.5000	0.00

TABLE 3. Results for different fault cases in presence of noise.

Test Case				F.L. error%	
Fault Type	δ_F°	L_{RF} (p.u.)	R_F (Ω)	With Noise	Without Noise
c_1g	180	0.3	20	0.03	0.03
a_1c_1	90	0.7	1	0.01	0.00
b_1c_1g	135	0.9	100	0.20	0.08
$a_1b_1c_1$	45	0.05	0.1	0.20	**0.21**
b_2g	0	0.15	5	**0.22**	0.04
b_2c_2	90	0.4	0.01	0.04	0.00
a_2c_2g	180	0.6	90	0.09	0.02
$a_2b_2c_2$	135	0.2	40	0.04	0.07
b_1g-c_2g	0	0.25	10	0.07	0.05
a_1g-b_2g	45	0.8	50	0.08	0.02
a_1b_1g- a_2c_2g	180	0.1	0.01	0.04	0.05
b_1c_1g- a_2b_2g	90	0.5	80	0.06	0.00

- Both proposed algorithm and [24] take into consideration the line shunt capacitance, while the scheme in [23] ignores the line shunt capacitance.
- Both schemes [23], [24] neglect the line asymmetry, while the proposed algorithm utilizes the line parameters in the phase-coordinates without the need for decoupling the double-circuit transmission line. Therefore, it can be applied for transposed or untransposed parallel lines.
- The proposed algorithm uses a lower sampling frequency (1200 Hz) compared with [23] and [24].
- Both proposed algorithm and [24] require the current samples at both line ends, while the scheme in [23] requires the voltage and current samples at both line ends.

TABLE 4. Comparative summary between proposed method and [23] & [24].

Item	Proposed	[23]	[24]
No. of circuits	Double-circuit	Single-circuit	
Line Model	Frequency-dependent	Lumped parameter	
Line shunt capacitance	Yes	No	Yes
Line asymmetry	Yes	No	No
Fs	0.12 kHz	20 kHz	200 kHz
Required Data	*I*	*V & I*	*I*
Fault type	All	3-phase	All
Line parameters errors	Yes	No	No

TABLE 5. F.L. error for proposed algorithm and [23] for different cases.

Test Case				F.L. error%	
Fault Type	δ_F°	L_{RF} (p.u.)	R_F (Ω)	Proposed	[23]
c_1g	180	0.3	20	0.03	0.09
a_1c_1	90	0.7	1	0.00	**2.30**
b_1c_1g	135	0.9	100	0.08	0.63
$a_1b_1c_1$	45	0.05	0.1	**0.21**	0.31
b_2g	0	0.15	5	0.04	0.65
b_2c_2	90	0.4	0.01	0.00	0.91
a_2c_2g	180	0.6	90	0.02	0.26
$a_2b_2c_2$	135	0.2	40	0.07	0.07
b_1g-c_2g	0	0.25	10	0.05	0.36
a_1g-b_2g	45	0.8	50	0.02	0.04
a_1b_1g- a_2c_2g	180	0.1	0.01	0.05	0.23
b_1c_1g- a_2b_2g	90	0.5	80	0.00	0.18

- The proposed algorithm is applicable for all fault types, including cross-circuit faults, while the scheme in [23] is only tested for 3-phase faults.
- The line parameters errors have a negligible influence on the proposed algorithm. In [23], [24], the derivation of both algorithms depends on the values of line parameters. However, the influence of line parameter errors is not evaluated in both algorithms.

For further illustration, the proposed fault location algorithm is compared with the scheme in [23] for the same fault cases in Table 1. The obtained results are depicted in Table 5. The maximum and average absolute percentage errors for all cases are respectively 0.21% and 0.048% for the proposed algorithm, while the maximum and average absolute percentage errors are respectively 2.30% and 0.5025% for the scheme in [23 CIRA- 2019-049]. As observed, the obtained results confirm that the proposed fault location algorithm is more accurate than the previous scheme in [23].

$$R = 10^{-3} \times \begin{bmatrix} 99.96 & 84.60 & 87.49 & 82.46 & 84.60 & 87.49 \\ 84.60 & 104.5 & 90.14 & 84.60 & 86.95 & 90.14 \\ 87.49 & 90.14 & 111.2 & 87.49 & 90.14 & 93.71 \\ 82.46 & 84.60 & 87.49 & 99.96 & 84.60 & 87.49 \\ 84.60 & 86.95 & 90.14 & 84.60 & 104.5 & 90.14 \\ 87.49 & 90.14 & 93.71 & 87.49 & 90.14 & 111.2 \end{bmatrix} (\Omega/km)$$

$$X_L = 10^{-2} \times \begin{bmatrix} 73.91 & 37.43 & 32.06 & 32.30 & 31.36 & 29.45 \\ 37.43 & 73.71 & 37.18 & 31.36 & 32.10 & 31.11 \\ 32.06 & 37.18 & 73.41 & 29.45 & 31.11 & 31.80 \\ 32.30 & 31.36 & 29.45 & 73.91 & 37.43 & 32.06 \\ 31.36 & 32.10 & 31.11 & 37.43 & 73.71 & 37.18 \\ 29.45 & 31.11 & 31.80 & 32.06 & 37.18 & 73.41 \end{bmatrix} (\Omega/km)$$

$$Y_C = 10^{-6} \times \begin{bmatrix} 3.64 & -0.81 & -0.33 & -0.36 & -0.25 & -0.17 \\ -0.81 & 3.77 & -0.82 & -0.25 & -0.29 & -0.26 \\ -0.33 & -0.82 & 3.61 & -0.17 & -0.26 & -0.38 \\ -0.36 & -0.25 & -0.17 & 3.64 & -0.81 & -0.33 \\ -0.25 & -0.29 & -0.26 & -0.81 & 3.77 & -0.82 \\ -0.17 & -0.26 & -0.38 & -0.33 & -0.82 & 3.61 \end{bmatrix} (S/km)$$

V. CONCLUSION

This article proposes a non-iterative time-domain fault location algorithm for double-circuit transmission lines connected to large scale wind farms. Only half-cycle of the synchronized current samples are used to obtain the locations of all fault types. Unlike existing techniques, the proposed fault location algorithm does not need any transformation technique to decouple the line. In addition, the proposed algorithm considers the effect of the line asymmetry, the mutual coupling, as well as the line shunt capacitance in fault equation derivation. Further, the fault distance is obtained directly by solving a non-iterative equation without any assumptions. The obtained results for the simulated cases on the PSCAD/EMTDC platform emphasize the high efficacy of the presented algorithm for fault resistance, fault location, as well as fault inception angle. In addition, the proposed fault location algorithm shows acceptable performance against cross-circuit faults, different sampling rates, line parameters errors, and synchronization and measurement errors. Further, the maximum percentage error is recorded to be 2.5% for all test cases, including the effect of the measurement errors.

APPENDIX

A. THE MAIN DATA OF THE WIND TURBINE GENERATOR

Parameter	Value
Rated power	5 MW
Rated stator voltage	0.69 kV
Rated frequency	60 Hz
Stator resistance	0.0054 p.u.
Rotor resistance	0.00607 p.u.
Stator leakage inductance	0.10 p.u.
Rotor leakage inductance	0.11 p.u.
Mutual inductance	0.02 p.u.
Magnetizing inductance	3.5 p.u.

B. THE CURRENT TRANSFORMERS DATA

Parameter	Value
Model	JA model
Ratio	1000/1 A
Burden impedance	2+0.3i Ω

C. THE SOURCE IMPEDANCE AT TERMINAL R

Sequence	Positive	Negative	Zero
Value	1.6+18.5i Ω	1.6+18.5i Ω	2.8+32.4i Ω

D. THE LINE PARAMETERS MATRICES (RESISTANCE, REACTANCE, AND ADMITTANCE) CONSIDERING THE UNTRANSPOSITION OF THE DOUBLE-CIRCUIT LINE

The equation as shown at the top of the page.

REFERENCES

[1] I. Kiaei and S. Lotfifard, "A two-stage fault location identification method in multiarea power grids using heterogeneous types of data," *IEEE Trans. Ind. Informat.*, vol. 15, no. 7, pp. 4010–4020, Jul. 2019.
[2] R. Liang, N. Peng, L. Zhou, X. Meng, Y. Hu, Y. Shen, and X. Xue, "Fault location method in power network by applying accurate information of arrival time differences of modal traveling waves," *IEEE Trans. Ind. Informat.*, vol. 16, no. 5, pp. 4010–4020, May 2020.
[3] M. M. Saha, J. J. Izykowski, and E. Rosolowski, *Fault Location on Power Networks*, 1st ed. London, U.K.: Springer, 2010.
[4] B. Mahamedi and J. G. Zhu, "Unsynchronized fault location based on the negative-sequence voltage magnitude for double-circuit transmission lines," *IEEE Trans. Power Del.*, vol. 29, no. 4, pp. 1901–1908, Aug. 2014.
[5] J. Ma, Y. Shi, W. Ma, and Z. Wang, "Location method for interline and grounded faults of double-circuit transmission lines based on distributed parameters," *IEEE Trans. Power Del.*, vol. 30, no. 3, pp. 1307–1316, Jun. 2015.

[6] N. I. Elkalashy, T. A. Kawady, W. M. Khater, and A.-M.-I. Taalab, "Unsynchronized fault-location technique for double-circuit transmission systems independent of line parameters," *IEEE Trans. Power Del.*, vol. 31, no. 4, pp. 1591–1600, Aug. 2016.
[7] A. Saber, A. Emam, and H. Elghazaly, "New fault location scheme for three-terminal untransposed parallel transmission lines," *Electr. Power Syst. Res.*, vol. 154, pp. 266–275, Jan. 2018.
[8] Y. Zhang, J. Liang, Z. Yun, and X. Dong, "A new fault-location algorithm for series-compensated double-circuit transmission lines based on the distributed parameter model," *IEEE Trans. Power Del.*, vol. 32, no. 6, pp. 2398–2407, Dec. 2017.
[9] A. Saber, A. Emam, and H. Elghazaly, "A backup protection technique for three-terminal multisection compound transmission lines," *IEEE Trans. Smart Grid*, vol. 9, no. 6, pp. 5653–5663, Nov. 2018.
[10] A. Ghorbani and H. Mehrjerdi, "Accurate fault location algorithm for shunt-compensated double circuit transmission lines using single end data," *Int. J. Electr. Power Energy Syst.*, vol. 116, Mar. 2020, Art. no. 105515.
[11] M. Kezunovic and B. Perunicic, "Synchronized sampling improves fault location," *IEEE Comput. Appl. Power*, vol. 8, no. 2, pp. 30–33, Apr. 1995.
[12] G. Song, J. Suonan, Q. Xu, P. Chen, and Y. Ge, "Parallel transmission lines fault location algorithm based on differential component net," *IEEE Trans. Power Del.*, vol. 20, no. 4, pp. 2396–2406, Oct. 2005.
[13] J. Morren and S. W. H. de Haan, "Short-circuit current of wind turbines with doubly fed induction generator," *IEEE Trans. Energy Convers.*, vol. 22, no. 1, pp. 174–180, Mar. 2007.
[14] K. Jia, Y. Li, Y. Fang, L. Zheng, T. Bi, and Q. Yang, "Transient current similarity based protection for wind farm transmission lines," *Appl. Energy*, vol. 225, pp. 42–51, Sep. 2018.
[15] A. Ahmadimanesh and S. M. Shahrtash, "Time–time-transform-based fault location algorithm for three-terminal transmission lines," *IET Gener., Transmiss. Distrib.*, vol. 7, no. 5, pp. 464–473, May 2013.
[16] M. Ghazizadeh-Ahsaee, "Time-domain based fault location for series compensated transmission lines without requiring fault type," *Electr. Power Syst. Res.*, vol. 181, Apr. 2020, Art. no. 106171.
[17] J. L. Suonan, G. B. Song, X. N. Kang, and S. G. Wang, "A time-domain fault location algorithm based on one-terminal current of parallel transmission lines," *Zhongguo Dianji Gongcheng Xuebao (Proc. Chin. Soc. Elect. Eng.)*, vol. 27, no. 7, pp. 52–57, 2007.
[18] A. K. Pradhan and G. Jos, "Adaptive distance relay setting for lines connecting wind farms," *IEEE Trans. Energy Convers.*, vol. 22, no. 1, pp. 206–213, Mar. 2007.
[19] A. Hooshyar, M. A. Azzouz, and E. F. El-Saadany, "Distance protection of lines connected to induction generator-based wind farms during balanced faults," *IEEE Trans. Sustain. Energy*, vol. 5, no. 4, pp. 1193–1203, Oct. 2014.
[20] L. A. Trujillo Guajardo, A. Conde Enríquez, and Z. Leonowicz, "Error compensation in distance relays caused by wind power plants in the power grid," *Electr. Power Syst. Res.*, vol. 106, pp. 109–119, Jan. 2014.
[21] S. Chen, N. Tai, C. Fan, J. Liu, and S. Hong, "Adaptive distance protection for grounded fault of lines connected with doubly-fed induction generators," *IET Gener., Transmiss. Distrib.*, vol. 11, no. 6, pp. 1513–1520, Apr. 2017.
[22] Y. Chen, M. Wen, X. Yin, Y. Cai, and J. Zheng, "Distance protection for transmission lines of DFIG-based wind power integration system," *Int. J. Electr. Power Energy Syst.*, vol. 100, pp. 438–448, Sep. 2018.
[23] M. M. A. M. Aly and M. A. H. El-Sayed, "Enhanced fault location algorithm for smart grid containing wind farm using wireless communication facilities," *IET Gener., Transmiss. Distrib.*, vol. 10, no. 9, pp. 2231–2239, Jun. 2016.
[24] B. Sahoo and S. R. Samantaray, "An enhanced fault detection and location estimation method for TCSC compensated line connecting wind farm," *Int. J. Electr. Power Energy Syst.*, vol. 96, pp. 432–441, Mar. 2018.
[25] R. Dubey, S. R. Samantaray, B. K. Panigrahi, and G. V. Venkoparao, "Adaptive distance relay setting for parallel transmission network connecting wind farms and UPFC," *Int. J. Electr. Power Energy Syst.*, vol. 65, pp. 113–123, Feb. 2015.
[26] M. Marcelino and S. Steven, *Transmission Expansion for Renewable Energy Scale-Up: Emerging Lessons and Recommendations*. Washington, DC, USA: A World Bank Study, 2012.
[27] WindEurope Associations. (Feb. 2020). *Wind Energy in Europe in 2019 Trends and Statistics*. [Online]. Available: https://windeurope.org/wp-content/uploads/files/about-wind/statistics/WindEurope-Annual-Statistics-2019.pdf
[28] (Jan. 18 2018). *Type 3 Wind Turbine Generator (WTG)*. [Online]. Available: https://www.pscad.com/knowledge-base/article/495
[29] (Feb. 14 2020). *HVDC VSC Transmission Linking An (Offshore) Islanded Wind Farm With (Onshore) AC Grid*. [Online]. Available: https://www.pscad.com/knowledge-base/article/223
[30] Z. Xu, M. Proctor, I. Voloh, and M. Lara, "CT saturation tolerance for 87L applications," in *Proc. 68th Annu. Conf. Protective Relay Eng.*, College Station, TX, USA, Mar. 2015, pp. 646–667.
[31] M. Davoudi, J. Sadeh, and E. Kamyab, "Transient-based fault location on three-terminal and tapped transmission lines not requiring line parameters," *IEEE Trans. Power Del.*, vol. 33, no. 1, pp. 179–188, Feb. 2018.

A. SABER received the B.Sc., M.Sc., and Ph.D. degrees in electrical power engineering from Cairo University, Giza, Egypt, in 2008, 2013, and 2019, respectively. He was a Visitor Researcher with Khalifa University, United Arab Emirates. He is currently an Assistant Professor with the Department of Electrical Power Engineering, Faculty of Engineering, Cairo University. His current research interests include HVAC and HVDC transmission system protection, microgrid protection, and distributed generation.

H. H. ZEINELDIN (Senior Member, IEEE) received the B.Sc. and M.Sc. degrees in electrical engineering from Cairo University, Giza, Egypt, in 1999 and 2002, respectively, and the Ph.D. degree in electrical and computer engineering from the University of Waterloo, Waterloo, ON, Canada, in 2006. He was with Smith and Andersen Electrical Engineering, Inc., North York, ON, USA, where he was involved in projects involving distribution system designs, protection, and distributed generation. He was a Visiting Professor with the Massachusetts Institute of Technology, Cambridge, MA, USA. He is currently with the Faculty of Engineering, Cairo University, Egypt, and on leave from Khalifa University, Abu Dhabi, United Arab Emirates. His current research interests include distribution system protection, distributed generation, and micro grids. He is currently an Editor of the IEEE TRANSACTIONS ON ENERGY CONVERSION.

TAREK H. M. EL-FOULY (Senior Member, IEEE) received the B.Sc. and M.Sc. degrees from Ain Shams University, Cairo, Egypt, in 1996 and 2002, respectively, and the Ph.D. degree in electrical engineering from the University Of Waterloo, Waterloo, ON, Canada, in 2008. He joined CanmetENERGY, Natural Resources Canada, in 2008, as a Transmission and Distribution Research Engineer. In 2010, he was appointed as an Adjunct Assistant Professor with the Department of Electrical and Computer Engineering, University of Waterloo. In 2014, he was promoted to a Smart Microgrids Research Manager at CanmetENERGY, Natural Resources Canada. In 2015, he joined as an Assistant Professor with the Department of Electrical and Computer Engineering, Khalifa University, where he was promoted to an Associate Professor in 2019. He conducts research on smart grids, microgrids, high penetration of renewable energy resources, and integration of electrical energy storage systems.

AHMED AL-DURRA (Senior Member, IEEE) received the Ph.D. degree in ECE from The Ohio State University in 2010. He is currently a Professor with the Department of EECS, Khalifa University, United Arab Emirates. He is leading the Energy Systems Control and Optimization Laboratory, Advanced Power and Energy Center. He has one U.S. patent. He has one edited book, 12 book chapters, and over 200 scientific articles in top-tier journals and refereed international conference proceedings. He has supervised/co-supervised over 25 Ph.D./master students. His research interests are applications of control and estimation theory on power systems stability, micro and smart grids, renewable energy systems and integration, and process control. He is an Editor of the IEEE TRANSACTIONS ON SUSTAINABLE ENERGY and the IEEE POWER ENGINEERING LETTERS and an Associate Editor of the IEEE TRANSACTIONS ON INDUSTRY APPLICATIONS, and *Frontiers in Energy Research*.